

Radio structure and variability of the extreme blazar AO 0235+164

A. M. Kutkin^{1*}, I. N. Pashchenko¹, M. M. Lisakov¹, P. A. Voytsik¹, K. V. Sokolovsky^{1,2,3}, Y. Y. Kovalev^{1,4}, A. P. Lobanov⁴, A. V. Ipatov⁵, M. F. Aller⁶, H. D. Aller⁶, A. Lahteenmaki^{7,8}, et al.

¹*Astro Space Center of Lebedev Physical Institute, Profsoyuznaya Str. 84/32, 117997 Moscow, Russia*

²*Sternberg Astronomical Institute, Moscow State University, Universitetskii pr. 13, 119992 Moscow, Russia*

³*IAASARS, National Observatory of Athens, Vas. Pavlou & I. Metaxa, 15236 Penteli, Greece*

⁴*Max-Planck-Institut für RadioAstronomie, Auf dem Hügel 69, D-53121 Bonn, Germany*

⁵*Institute of Applied Astronomy of the Russian Academy of Sciences, 191187, Kutuzov embankment, 10, St. Petersburg, Russia*

⁶*University of Michigan, Astronomy Department, Ann Arbor, MI 48109-1042 USA*

⁷*Aalto University Metsähovi Radio Observatory, 114, Kylmälä, 02540, Finland*

⁸*Department of Radio Science and Engineering, 13000, FI-00076 AALTO, Finland*

Accepted 2017 XXXXX XX. Received 2017 XXXXX XX; in original form 2017 XXXXX XX

ABSTRACT

Clues on physical conditions in radio cores of blazars come from measurements of brightness temperatures as well as effects produced by intrinsic opacity. We study the properties of ultra compact blazar AO 0235+164 with RadioAstron Space-VLBI, multi-frequency VLBA, EVN and single-dish radio observations. We employ visibility modeling and image stacking for deriving structure and kinematics of the source, and use Gaussian process regression to find relative multi-band time delays of the flares. The apparent core size at cm/mm wavelengths depends on frequency as $W = \nu^{-0.8 \pm 0.1}$ implying the photosphere interpretation of the core with prevailing synchrotron self absorption. Variability time delays agree with this scenario, while the power index differs significantly for individual flares. The intrinsic brightness temperature in the core, derived from ground-based VLBI, is close to the equipartition regime value. We find that the jet of AO 0235+164 has moderate Doppler and Lorentz factors. There is an evidence for ultra-compact ($< 10 \mu\text{as}$) features in the source, which might be responsible for the extreme apparent brightness temperatures $T_b > 10^{13} \text{ K}$ measured earlier by VSOP and confirmed recently by RadioAstron space interferometers. In 2007–2016 the VLBI components in the source at 43 GHz are found predominantly in two directions. Brighter and more compact ones reside to the south, while fainter and larger are to the north of the core. We suggest that this structure is caused by the bent of the outflow from southern to northern direction. The apparent opening angle of the jet seen in stacked image at 7 mm $\varphi = 60^\circ$ is two times larger than one measured by MOJAVE at 2 cm, implying a collimation of the flow within central 1.5 mas. Intrinsic opening angle $\varphi_{int} = 2^\circ$ is close to the viewing angle of the jet $\theta = 1.7^\circ$. The core at 7 mm is about ten parsecs downstream from the jet apex and has magnetic field strength $B \approx 0.1 \text{ G}$.

Key words: galaxies: active – galaxies: BL Lac – individual – 0235+164: jets – radio continuum: jets – core shift: jets – variability time lags

1 INTRODUCTION

Blazars are jetted active galactic nuclei (AGN) viewed at a small angle to the line of sight. They appear on very

long baseline interferometry (VLBI) images as unresolved or barely resolved bright core often accompanied by one-sided jet. Radio emission is produced via synchrotron mechanism and is boosted by relativistic effects. The core has a flat or inverted spectrum at cm/mm wavelengths and is usually associated with emission from a surface of unit optical

* E-mail:kutkin@asc.rssi.ru

depth (Blandford & Königl 1979), while alternative interpretations exist (Marscher 2006, 2008). Strong support for the former interpretation comes from the shift between the apparent core positions measured at different frequencies, first detected by Marcaide & Shapiro (1984). In the framework of this model, the measured core shift may be used to probe jet physics in the core region including magnetic field strength and its distribution along the outflow, linear scales of the jet, its kinetic energy, etc. (Lobanov 1998, Hirotani 2005).

Core shift can be measured directly when a source has prominent jet, so that one can use its optically thin features as a reference. There is also an astrometrical way to measure core shift using nearby sources for reference (e.g. Hada et al. 2011). For a compact source the core shift can be estimated indirectly. Opacity is also responsible for changing of the angular size of the apparent core measured at different frequencies. Therefore the core size frequency dependence can be linked to the core shift within assumptions about geometry of a jet. Moreover, these measurements allow one to distinguish between intrinsic absorption and scattering in the interstellar medium (e.g. Pushkarev & Kovalev 2015). Finally, the time delays between single-dish light curves at radio bands might also reflect the offset between the core at these frequencies and the outflow velocity (Kudryavtseva et al. 2011, Kutkin et al. 2014).

The radio source AO 0235+164 (hereafter 0235+164; 02:38:38.930107 +16:36:59.27460¹, J2000) was classified as a BL Lac-type object by Spinrad & Smith (1975) on the basis of its variability and optical spectrum that appeared featureless at low spectral resolution (Véron-Cetty & Véron 2010 classify the object as QSO based on its absolute magnitude). Cohen et al. (1987) measured the object's redshift detecting Mg II, [Ne V] and [O II] lines at $z = 0.94$. They also found intervening absorption and emission features at lower redshifts. The blazar resides in a field of many faint foreground galaxies (Burbidge et al. 1996, Nilsson et al. 1996) with $z \sim 0.5$, and often considered to be affected by gravitational lensing (Stickel et al. 1988, Abraham et al. 1993, Webb et al. 2000).

As seen by VLBI, the source is partially resolved at most radio bands, however its extended structure is very unstable. Sometimes, it is not detected (Gabuzda & Cawthorne 2000), other times there are components at different position angles and various resolution scales (see e.g. Jones et al. 1984, Altschuler et al. 1995, Chu et al. 1996, and references therein). Jorstad et al. (2001) reported jet northwest of the core seen by 7mm VLBA. Later VLBA monitoring revealed temporary occurrence of a component located south-southeast of the core (Agudo et al. 2011, this paper).

The blazar 0235+164 is one of the few most bright sources detected by VSOP and RadioAstron space-VLBI missions. Based on VSOP measurements, its brightness temperature is reported to reach $T_b \approx 10^{13.8}$ K (Frey et al. 2000), which challenges the inverse Compton limit even after being corrected for boosting with extremely high Doppler factors.

The source demonstrates violent variability across the electromagnetic spectrum on timescales from hours to years (e.g. Ackermann et al. 2012 and references in their introduc-

tion). The observed cm-wavelength flux density of 0235+164 increases up to 6–7 times during the flaring states. The short-term variability at lower frequencies might be produced by interstellar scintillations of newborn ultra-compact VLBI components with a size about 10 μas (Rickett et al. 2006). These blobs, in turn, might be responsible for the extremely high brightness temperatures in the source.

In this paper we analyze both VLBI (including Space-VLBI RadioAstron data) and single-dish total flux radio observations of 0235+164 in order to shed more light on structure and variability of this enigmatic source. The observations are summarized in Section 2. In Sections 3–4 we describe the methods used for VLBI-data and light curves analysis. Multi-frequency time lags and core size are discussed in Sections 5–6. Section 7 contains derivation of brightness temperature and Doppler factor as well as RadioAstron measurements. In Sections 8–9 we discuss jet structure and estimate its physical and geometrical parameters.

We adopt the standard ΛCDM cosmology model with $H_0 = 71 \text{ km s}^{-1} \text{ Mpc}^{-1}$, $\Omega_m = 0.27$, and $\Omega_\Lambda = 0.73$ (Komatsu et al. 2009), which corresponds to a luminosity distance $D_L = 6141.3 \text{ Mpc}$, an angular size distance $D_A = 1631.8 \text{ Mpc}$, and a linear scale of 7.91 pc mas^{-1} at the source redshift. We use positively-defined spectral index $\alpha = d \ln S / d \ln \nu$.

2 OBSERVATIONAL DATA

2.1 Ground-based VLBI observations

The blazar 0235+164 was observed on 2 September 2008 with the Very Long Baseline Array² (VLBA; Napier 1994), a network of ten identical 25-m antennas spread across the US providing baselines of up to 8600 km. The VLBA's frequency agility was used to perform imaging simultaneously at seven frequencies (4.6/5.0, 8.1/8.4, 15.4, 23.8, and 43.2 GHz). Eight 8 MHz-wide frequency channels (IFs) were recorded at 128 Mbps with 1-bit sampling. The 5 and 8 GHz data were split into two sub-bands (four IFs each) to provide independent measurements at close frequencies. The observation included 13 on-source scans (each 3–7 minutes long depending on frequency) spread over 8 hours. The data were correlated at the NRAO Array Operation Center in Socorro, NM. This observation was conducted in the framework of our survey of parsec-scale radio spectra of twenty γ -ray bright blazars (Sokolovsky et al. 2010a,b).

Another set of multi-frequency observations was performed by the European VLBI Network at S/X bands (2.3 and 8.4 GHz) on 19 October 2008, C (5 GHz) on 22 October 2008 and L (1.7 GHz) on 29 October 2008. Each band included 8 IFs of 8 MHz width. C and L bands were recorded in right and left circular polarizations, while S and X bands – in the right one with a full bitrate of 512 Mbit/s. The correlation was performed at the Joint Institute for VLBI ERIC (Keimpema et al. 2015).

The a priori amplitude calibration, phase calibration with the phase-cal signal injected during observations, fringe

¹ http://astrokeo.org/vlbi/solutions/rfc_2016c/

² <https://science.nrao.edu/facilities/vlba>

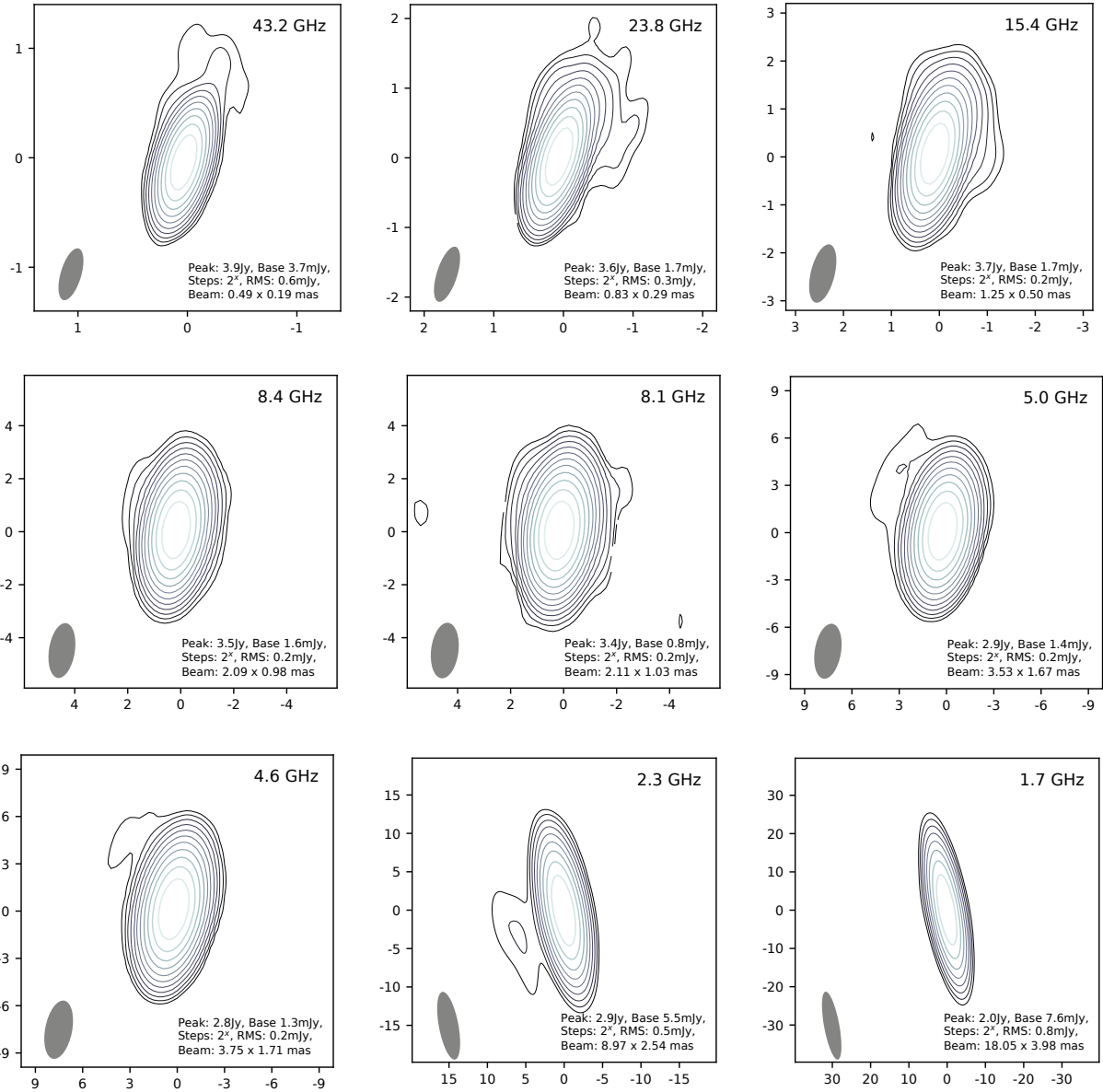


Figure 1. 0235+164 clean maps in RA-Dec axes. The beam size (at half maximum) is plotted in the lower left corner.

fitting (performed separately for each IF) and bandpass correction were applied in AIPS (Greisen 1990). The hybrid imaging (Walker 1995) including iterations of image deconvolution using the CLEAN algorithm (Högbom 1974) followed by amplitude and phase self-calibration were performed in Difmap (Shepherd 1997). We applied a special procedure involving preliminary imaging used to determine residual antenna gain corrections that are persistent in time and appear for all the observed sources (a similar procedure was utilized by Sokolovsky et al. 2011). The resulting amplitude calibration accuracy is expected to be $\sim 5\%$ in the 4.6–15.4 GHz range and $\sim 10\%$ at 23.8 and 43.2 GHz. Details of the employed calibration and analysis technique are described by Sokolovsky (2011).

The clean maps of 0235+164 at different frequencies are

shown in Figure 1. Both multi-frequency experiments fall on the prominent radio flare in the source.

We also analyze the calibrated VLBA UV-data at 43 GHz by Boston University blazar group³ covering 2007–2016 (100 observational epochs). The imaging and model fitting procedures are performed in the same manner as for the multi-frequency data.

2.2 Single-dish total flux density observations

The single-dish flux density monitoring observations (Figure 2) of 0235+164 were obtained with the 26-m radio telescope of University of Michigan Radio Observa-

³ http://www.bu.edu/blazars/VLBA_GLAST/0235.html

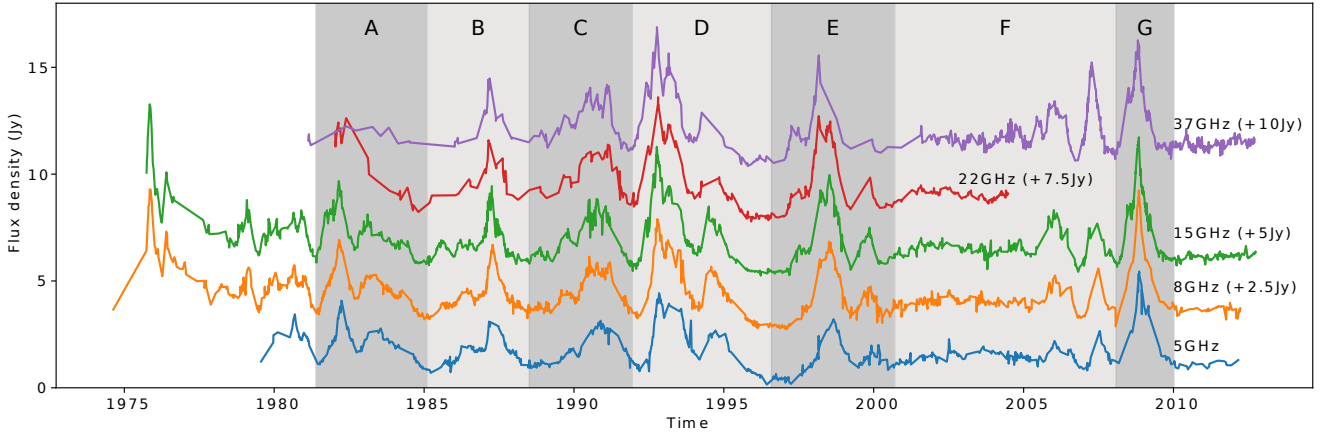


Figure 2. The single-dish light curves of AO 0235+164 at 4.8 – 37 GHz (shifted along y-axis for better visualization). Shaded areas denote the epochs of interest (see Section 4 for details).

tory⁴ (UMRAO) at 4.8, 8.0 and 14.5 GHz, 40-m telescope of Owens Valley Radio Observatory⁵ (OVRO) at 15 GHz (Richards et al. 2011), and 14-m telescope of Metsähovi Radio Observatory⁶ telescope at 22 and 37 GHz. For the subsequent analysis we merge the complementary 15 GHz data by OVRO and UMRAO.

2.3 RadioAstron space-VLBI observations

The blazar 0235+164 is a target of RadioAstron AGN survey (Kovalev et al., in prep.). It is monitored regularly at L (1.6 GHz), C (4.8 GHz) and K (22.2 GHz) bands by the space radio telescope antenna along with ground-based telescopes in interferometric mode. A typical observational set covers 40–60 minutes and is performed either in a single band with two circular polarizations or in two bands with one circular polarization of opposite sense per band. Correlation is performed at the Astro Space Center using software correlator (Kardashev et al. 2013, Likhachev et al. 2017). Post correlation handling (fringe fitting, calibrations) is performed using PIMA⁷ software (Petrov et al. 2011). We analyze 12 observational epochs from Dec 2012 through Jan 2016, as summarized in Table 3.

3 VLBI ANALYSIS

We model the VLBI structure of 0235+164 at each frequency with elliptical (the core) and circular Gaussian component(s) in the uv -plane using **Difmap**. We choose elliptical core based on comparison of this model with point source and circular Gaussian models using the K -fold cross-validation criteria (Hastie et al. 2009). In this approach the data on each baseline are divided randomly into K sets, then the models are re-fitted to $K - 1$ sets and their predictions

on the K -th set are compared. The model with minimal residuals is then selected. We also vary $K \in [3, 10]$ for the sake of robustness. The elliptical model is found to better describe the data. The extended structure, if any, is weak and does not affect core parameters significantly. The errors of model parameters are estimated in the image plane following Fomalont (1999).

Additionally we compare the size of the fitted core with the resolution limit suggested by Kovalev et al. (2005) for a Gaussian brightness distribution template. The core is resolved at all frequencies except for 1.7 GHz and almost at all epochs of the 7 mm long-term monitoring data. If the core is unresolved, we use the corresponding resolution limit for its major and minor axes size. Models for the multi-frequency experiments are summarized in Table 1.

4 LIGHT CURVES ANALYSIS

The variability time delays between light curves can be found using several methods based either on data modeling or cross-correlation techniques. The former implies some prior knowledge about the data (e.g. Gaussian shapes of the flares (Pyatunina et al. (2007), Kudryavtseva et al. (2011) or two-sided exponential profiles (Valtaoja et al. (1999), Hovatta et al. (2009))). Moreover, one has to divide a light curve into separate flares, which is the subject of errors due to human factor. The latter methods are based on calculation of mutual cross-correlation function (CCF) of the light curves and do not involve additional information about their structure (e.g. standard correlation function with interpolation (ICCF) or discrete correlation function (DCF; Edelson & Krolik (1988))). However these methods require sufficient amount of data to perform well and also imply some parameters which may affect the results, like the size of the bin used for interpolation or for DCF evaluation (see White & Peterson (1994) for ICCF/DCF comparison and references).

Another approach, which also does not require any prior knowledge about the data is based on the Gaussian process regression (GPR; Rasmussen & Williams 2005) – a special case of Bayesian non-parametric models. It has been recently

⁴ <http://lsa.umich.edu/astro>

⁵ <http://www.astro.caltech.edu/ovroblazars/>

⁶ <http://metsahovi.aalto.fi/en/>

⁷ <http://astrogeo.org/pima>

Table 1. Source models for the two multi-frequency experiments. Columns: (1) – frequency, (2) – component ID, (3–8) – standard Difmap format: Flux, Distance, Position angle, Major axis, Axial ratio, Major axis orientation angle.

Freq. (GHz)	ID (2)	S (Jy) (3)	R (mas) (4)	θ_c (deg) (5)	b_{maj} (mas) (6)	e (7)	Φ (deg) (8)
(1)							
43.2	C0	3.498	0.027	171	0.058	0.56	7.7
	C1	0.636	0.146	-178	0.064		
	C2	0.051	0.149	113	< 0.001		
	C3	0.062	0.613	-18	0.837		
23.8	C0	3.714	0.015	2	0.115	0.43	24.0
	C1	0.046	0.204	88	0.174		
	C2	0.110	0.634	-22	0.714		
15.37	C0	3.714	0.059	-2	0.125	0.50	28.0
	C1	0.163	0.725	-18	0.821		
8.43	C0	3.378	0.038	-28	0.197	0.56	-13.6
	C1	0.258	0.686	-23	0.802		
8.11	C0	3.288	0.035	-51	0.196	0.45	-26.3
	C1	0.247	0.729	-23	0.772		
5.0	C0	2.758	0.057	-42	0.328	0.57	-10.9
	C1	0.288	0.669	-22	1.127		
4.61	C0	2.642	0.097	-39	0.346	0.51	-16.8
	C1	0.297	0.678	-22	1.189		
8.39	C0	6.457	0.049	-173	0.197	0.56	5.0
	C1	0.374	0.447	-21	0.655		
	C2	0.015	1.550	79	1.001		
4.97	C0	4.897	0.032	143	0.290	0.46	0.7
	C1	0.414	0.588	-16	1.003		
2.27	C0	2.987	0.057	-163	0.772	0.73	-11.0
	C1	0.015	2.864	-48	< 0.001		
	C2	0.037	6.164	112	5.684		
1.66	C0	2.069	0.093	19	< 1.590	0.60	2.1
	C1	0.010	4.315	61	< 0.001		
	C2	0.010	4.902	-24	0.009		

applied to the light curves of the blazar PKS 1502+106 by Karamanavis et al. (2016).

Gaussian process (GP) is a probability distribution over functions. It is characterized by its mean value and covariance matrix. The former can be set to zero by shifting the data, the latter is expressed through covariance function (*kernel*). The kernel depends on *hyperparameters*, which are determined for given data by maximizing marginal likelihood function (*training* the GP).

The often used kernel for time series is “squared exponential” (SE):

$$C_{SE}(x_i, x_j) = A^2 \exp\left(\frac{-(x_i - x_j)^2}{2l^2}\right), \quad (1)$$

where l is the characteristic scale indicating the connection between x_i and x_j , and A reflects the distribution of function values around the mean.

In case of longer light curves containing several or multi-peaked flares the single SE kernel (1) might not perform well

due to a presence of more than one characteristic scales in the source variability. This is the case for blazars, which are known to vary on a range of timescales and usually possess “red” power spectra (e.g. Max-Moerbeck et al. 2014, and references therein). To overcome this problem one may use a sum of several SE-kernels. Such a weighted sum is represented by the rational quadratic (RQ) kernel (Rasmussen & Williams 2005, Chapter 4):

$$C_{RQ}(x_i, x_j) = A^2 \left(1 + \frac{(x_i - x_j)^2}{(2\varepsilon l^2)}\right)^{-\varepsilon} \quad (2)$$

The relative weighting of different time scales variations is specified by hyper parameter $\varepsilon \in (0, +\infty)$. In the limit of $\varepsilon \rightarrow +\infty$ the RQ kernel becomes an SE kernel.

We use the kernel represented by a sum of RQ-kernel and one characterizing white noise:

$$C(x_i, x_j) = C_{RQ}(x_i, x_j) + (x_i - x_j)\sigma_n^2 \quad (3)$$

with the hyperparameters A, l, α of RQ-kernel and σ_n , which characterizes random noise of the observed data. We also take into account the uncertainties of estimated hyperparameters by integrating the distributions along corresponding axes (MacKay 2003).

In order to check whether there is a difference between time lags on different epochs we split our data into seven time intervals each having at least one flare and containing more or less sufficient data for analysis. The selected intervals are denoted in Figure 2.

GPR is performed using `george` python library (Am-bikasaran et al. 2014). For sampling the posterior distributions of hyperparameters we employ `emcee` Markov chain Monte Carlo (MCMC) sampler (Foreman-Mackey et al. 2013).

From the obtained posterior distributions we estimate time and flux density of each flare peak. These results are summarized in Table 2. Separate flares and the corresponding time delays are shown in Figure 4.

As an example, the results of implementing GPR to the 15 GHz light curve of epochs interval 1985 – 1988 (labeled B) are shown in Figure 3. The histograms illustrate the obtained posterior distributions of hyperparameters (the plot is produced with `corner` package by Foreman-Mackey 2016). Median and 16/84 percentiles are shown by vertical lines. In the upper right corner the light curve is shown along with $\pm 3\sigma$ (99.7%) confidence interval for GPR. Note the outlier data point near the flare peak which is effectively bypassed by GPR, but certainly would be a challenge for cross-correlation methods. As expected, the confidence interval widens within data gaps.

We also apply the DCF method to the time intervals labeled in Figure 2. In order to estimate the errors of the obtained delays we perform Monte Carlo simulations and modified bootstrapping or flux randomization / random subsample selection (FR/RSS) method proposed by Peterson et al. 1998). This allows us to account for errors due to initial flux measurements uncertainties as well as for possible outliers in the data. To account for the possible influence of the selected time bin we vary it in each simulation to be uniformly spread in the range $[0.5, 1.5]\Delta t_{mean}$ (where Δt_{mean} is the mean time span between the observations.

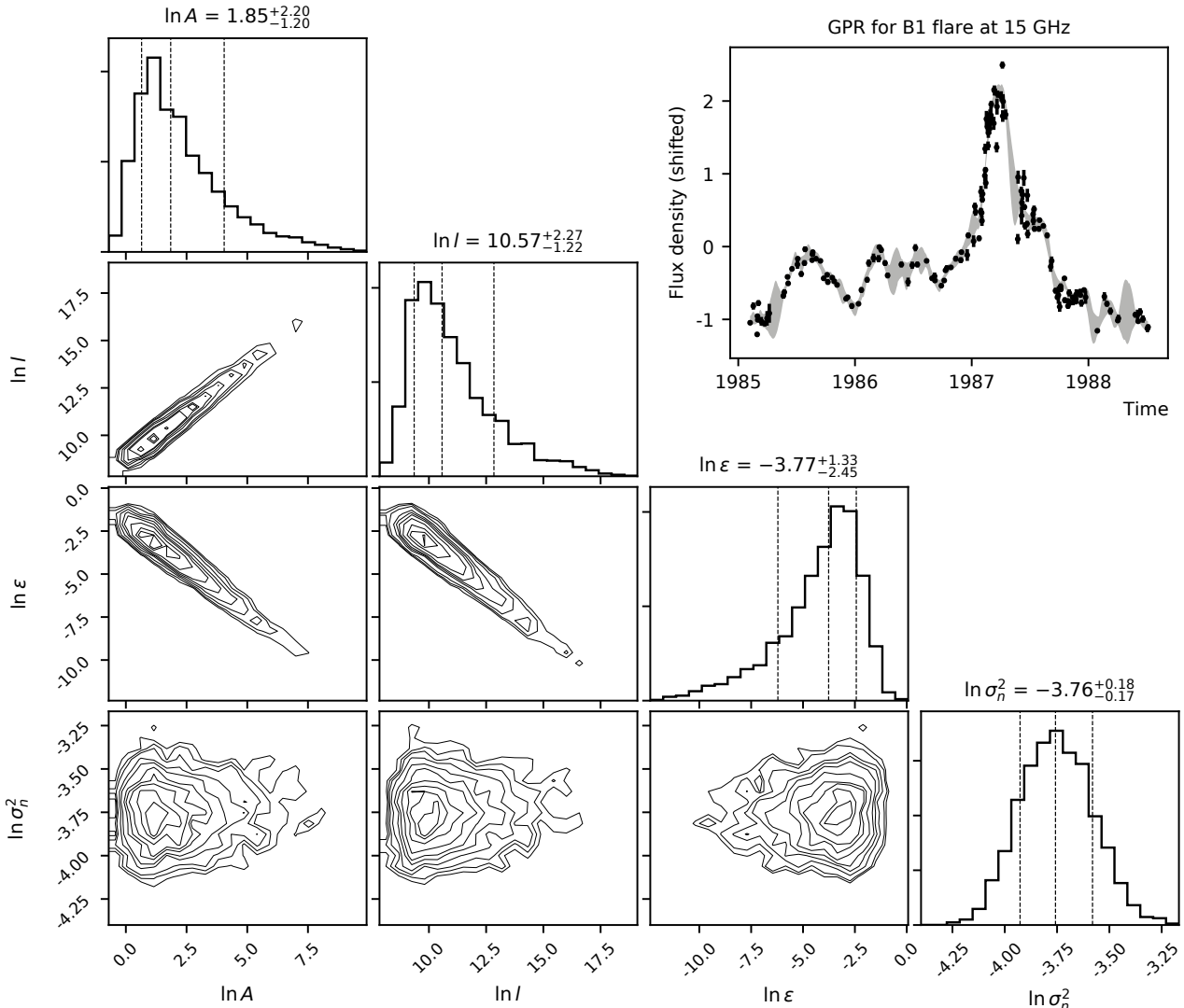


Figure 3. Application of GPR to the 15 GHz B-flare: the posterior distributions of GP hyperparameters (dashed lines indicate 16, 50 and 84 percentiles). The light curve with mean flux density subtracted is shown in the upper right corner, shaded area denotes $\pm 3\sigma$ confidence interval of GPR.

The obtained results are similar to GPR but have huge uncertainties, which makes their further analysis impractical. The following discussion is based on the results obtained with the GPR method.

5 VARIABILITY TIME DELAYS

We approximate dependence of the time lags ΔT on frequency ν (comparative to the peak at highest one) with model $\Delta T = a_t \nu^{-k_t} + b_t$. The `emcee` MCMC sampler is used with uniform prior distributions for a_t and b_t and normal prior distribution for index $k_t = 0.90 \pm 0.44$ (Pushkarev & Kovalev 2015). We assume here that the observed time lags between flares peaks at different frequencies are caused by the same intrinsic opacity mechanism, which is responsible for the core shift (and changing of the core size) effect, i.e. synchrotron self-absorption. This assumption is used to set

the aforementioned prior distribution for the sought parameter k_t . Parameter $b_t < 0$ corresponds to the delay between flare at a given highest frequency and "infinite" frequency, $a_t > 0$ characterizes jet velocity, and k_t reflects the opacity mechanism and geometry of the jet. It also can be connected with the distributions of magnetic field strength and particle density along the jet.

As seen in Figure 4 the obtained peak-to-peak delays differ from one flare to another. Moreover, there are flares with unusual lags when a peak comes earlier on lower frequency. (Table 2). Similar unexpected time delays in the source have been reported by Kraus et al. (1999) for short flare in 1992 which is a part of D-flare in our notation.

We obtain a wide range of parameter $k_t \in [0.7; 1.8]$ with median value $k_t = 1.2$. The posterior k_t distributions are plotted on Figure 5 for the two marginal cases (D1-flare with $k_t = 1.8$ and F2-flare with $k_t = 0.7$), showing the difference between obtained k_t with confidence more than 95%. We

Table 2. GPR results: the peak time (T_m , MJD) and flux density (F_m , Jy) of the flares at 37 – 5 GHz. The values are median, 84/16 percentiles (and median absolute deviation in brackets).

		37 GHz	22 GHz	15 GHz	8 GHz	4.8 GHz
A1	T_m	$45030^{+2}_{-1}(1.4)$	$45034^{+2}_{-2}(1.8)$	$45057^{+6}_{-5}(5.9)$
	F_m	$4.53^{+0.04}_{-0.04}$	$4.30^{+0.02}_{-0.03}$	$3.65^{+0.07}_{-0.06}$
B1	T_m	$46866^{+14}_{-9}(10.3)$	$46857^{+5}_{-17}(8.8)$	$46888^{+8}_{-3}(5.5)$	$46900^{+3}_{-3}(2.9)$	$46913^{+15}_{-8}(11.9)$
	F_m	$4.49^{+0.22}_{-0.14}$	$4.15^{+0.21}_{-0.13}$	$4.09^{+0.03}_{-0.04}$	$4.01^{+0.05}_{-0.05}$	$3.32^{+0.19}_{-0.21}$
D1	T_m	$48904^{+4}_{-3}(3.4)$	$48912^{+5}_{-4}(5.1)$	$48903^{+1}_{-1}(0.9)$	$48911^{+1}_{-1}(1.1)$	$48930^{+1}_{-4}(2.2)$
	F_m	$6.70^{+0.13}_{-0.11}$	$5.84^{+0.10}_{-0.09}$	$6.11^{+0.04}_{-0.05}$	$5.31^{+0.04}_{-0.04}$	$4.17^{+0.02}_{-0.02}$
E1	T_m	$50873^{+3}_{-3}(2.8)$	$50876^{+3}_{-2}(2.4)$	$50907^{+10}_{-8}(9.1)$
	F_m	$5.30^{+0.13}_{-0.10}$	$5.08^{+0.07}_{-0.07}$	$4.01^{+0.07}_{-0.07}$
E2	T_m	...	$51001^{+5}_{-8}(6.6)$	$51015^{+4}_{-3}(3.8)$	$51008^{+2}_{-2}(2.1)$	$51027^{+7}_{-10}(8.0)$
	F_m	...	$4.80^{+0.14}_{-0.14}$	$4.56^{+0.15}_{-0.15}$	$4.18^{+0.04}_{-0.05}$	$3.25^{+0.03}_{-0.05}$
E3	T_m	$51492^{+1}_{-2}(1.6)$	$51496^{+7}_{-5}(6.2)$	$51530^{+3}_{-4}(3.7)$
	F_m	$2.30^{+0.02}_{-0.02}$	$2.02^{+0.05}_{-0.04}$	$1.66^{+0.02}_{-0.01}$
F1	T_m	$53723^{+9}_{-13}(11.7)$...	$53752^{+7}_{-6}(6.3)$	$53763^{+5}_{-4}(4.6)$	$53752^{+1}_{-2}(1.5)$
	F_m	$3.42^{+0.12}_{-0.13}$...	$3.26^{+0.04}_{-0.04}$	$2.62^{+0.04}_{-0.04}$	$2.06^{+0.02}_{-0.01}$
F2	T_m	$54203^{+4}_{-4}(3.7)$...	$54251^{+14}_{-12}(13.1)$	$54269^{+6}_{-8}(7.3)$	$54290^{+7}_{-6}(6.8)$
	F_m	$4.96^{+0.11}_{-0.11}$...	$2.78^{+0.14}_{-0.09}$	$3.09^{+0.08}_{-0.07}$	$2.39^{+0.09}_{-0.09}$
G1	T_m	$54764^{+3}_{-2}(2.7)$...	$54770^{+1}_{-0}(1)$	$54774^{+1}_{-2}(1.2)$	$54784^{+2}_{-1}(1.9)$
	F_m	$6.00^{+0.12}_{-0.13}$...	$6.48^{+0.03}_{-0.03}$	$6.57^{+0.05}_{-0.05}$	$5.37^{+0.06}_{-0.07}$

find no correlation between k_t and peak flux density for the flares, neither somewhat monotonic changing of k_t in time.

Different values of index k_t within one source for separate flares have been also reported by Kudryavtseva et al. (2011). The reason for its changing is not obvious, and may be related either to measurements uncertainties due to lack of data or intrinsic changes in the jet, e.g. when the injected particles distort the profile of initial electron distribution of a steady outflow.

On the last panel of Figure 4 the light curves of 37 GHz single dish, 43 GHz core and 43 GHz superluminal component G_c are shown (see also § 8.2). Peak-to-peak time delay between the component and the core flares obtained using GPR is $T_{Gc,max} - T_{Core,max} = 21 \pm 4$ days. One can see, that the total flux measured by single-dish telescope is a sum of the core and G_c and has maximum somewhere in the middle between their peaks. Obviously, this yields to incorrect interpretation of the single-dish flare peak as a passage time of a disturbance through the core, and may be responsible for the different values of k_t .

Another noticeable effect is that the profile of the total

flux is much smoother than the profile of the core flare. But the former is often treated as the latter and used for brightness temperature and Doppler factor estimates. In this case there must be a bias due to overestimation of the variability time scale. The light curve of the core flare differs from a typical single-dish light curve: it has smoother raise and steeper decay. Therefore, the variability time scale may differ for different spatial resolution (see also section 7).

6 CORE SIZE AND SPECTRUM

Apparent size of a VLBI core depends on observations frequency. The photosphere interpretation assumes that this dependency follows the same power law as for the core shift (i.e. $W_{core} \propto \nu^{k_w}$, with k_w close to 1). This was shown for simultaneous multi-frequency observations by Kutkin et al. (2014) for blazar 3C 454.3 and derived statistically for large AGN samples by Yang et al. (2009) ($k_w = -0.95 \pm 0.37$) and by Pushkarev & Kovalev (2015) ($k_w = -0.90 \pm 0.44$) for the sources located at Galaxy latitudes higher than $\sim 10^\circ$,

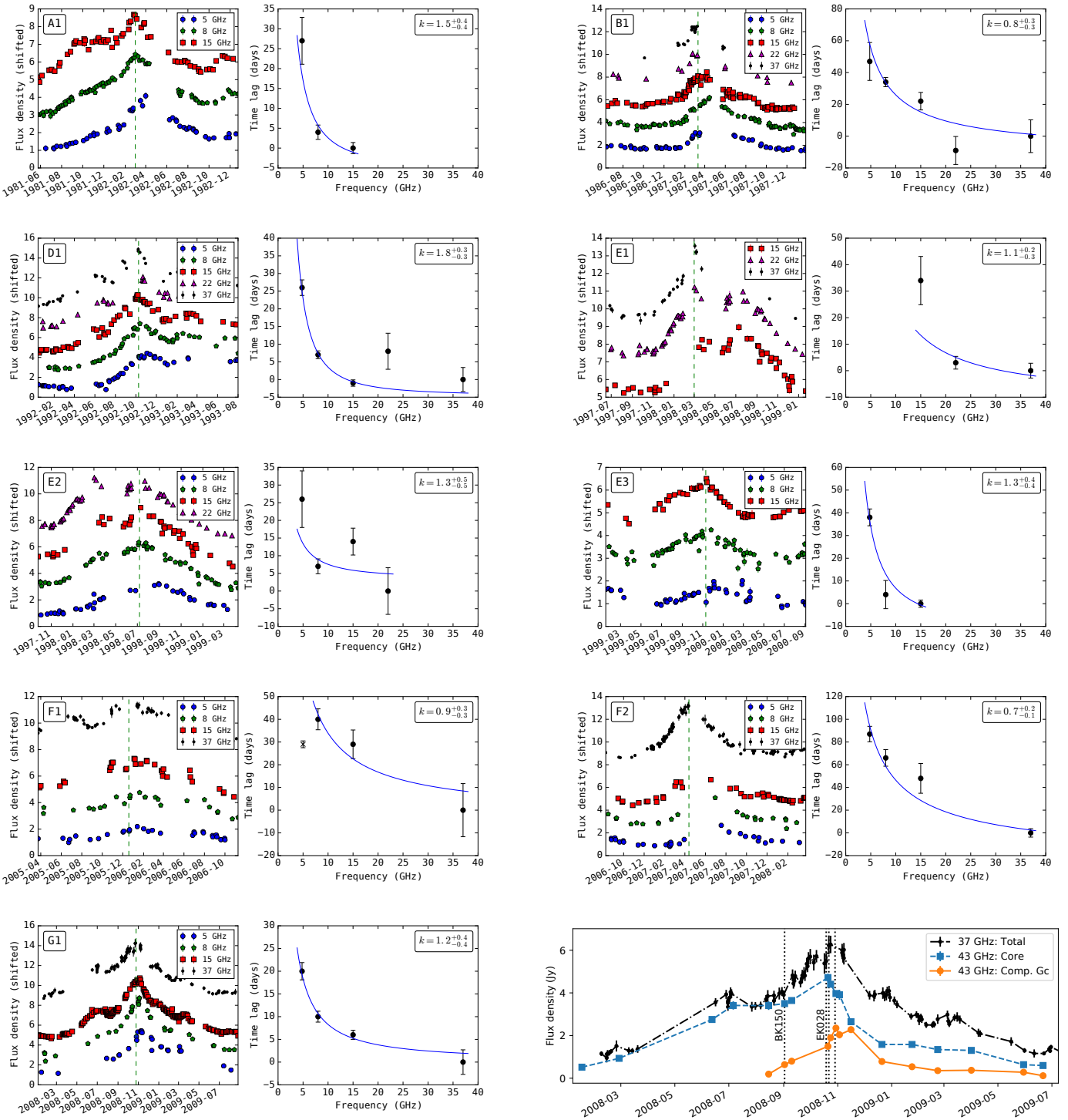


Figure 4. Plots of separate flares and the corresponding time lags. Vertical dashed lines mark the peak time at highest frequency. The last panel shows light curves of single-dish 37 GHz, the core, and the component Gc. Multi-frequency VLBI experiments marked with vertical dotted lines.

while for Galactic plane residents the power index is closer to $k_w \approx -2$ due to interstellar scattering.

The core in both multi-frequency VLBI experiments is modeled with an elliptical Gaussian with the mean axial ratio $\epsilon \sim 0.5$ (see Table 1). The dependence of its major

and minor axes (FWHM of the Gaussian) on frequency is approximated with the model $W(\nu) = a_w \nu^{-k_w}$ (an absence of an additional constant term here suggests that the core has “zero” size at “infinite” frequency). Since there is no significant difference between the core size obtained from

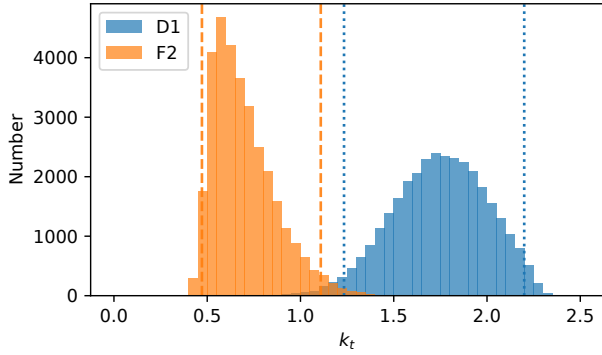


Figure 5. Posterior distributions of k_t parameter for D1 and F2 flares. Vertical dotted and dashed lines denote corresponding 95% intervals.

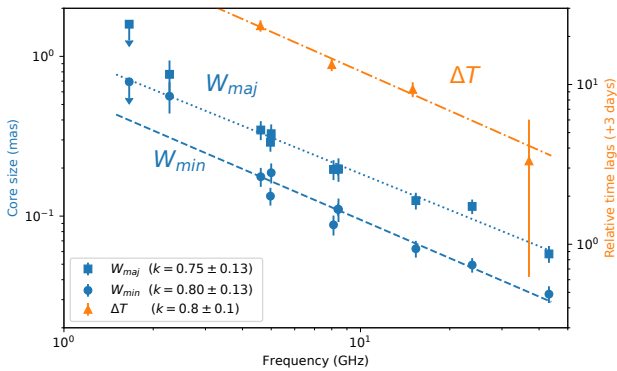


Figure 6. The core size W (left axis) and the time lags of the G-flare peaks ΔT (right axis) vs. observations frequency.

two VLBI experiments at 5 and 8 GHz, we merge these data for a better fit representation (see Figure 6).

Both major and minor axes follow the power law with $k_{w,maj} = k_{w,min} = 0.8 \pm 0.1$ ($a_{w,maj} = 1.1 \pm 0.1$, $a_{w,min} = 0.65 \pm 0.07$), which is in good agreement with the photosphere scenario. Since the modeled core size at L-band does not fulfill the resolution criteria, the upper limit is used. The core at S-band (2.3 GHz) is formally resolved, however, its size is larger than expected from synchrotron self absorption model. To check whether there is an interstellar scattering coming into play on these frequencies we find the corresponding angular broadening for the given celestial position ($\Theta_S = 0.16$ mas) from the NE2001 model (Cordes & Lazio 2002). This is significantly lower than the core size obtained from modeling, suggesting either that the scattering is not implicated here or there is really much denser Galactic medium at that direction. We also note, that excluding the data at L and S bands does not affect results of the fit.

The power index found for the core size k_w coincides within the errors with one obtained for the time lags but is measured with much better accuracy. Therefore, the former can be used to constrain the latter and other model-fit parameters of the time lags dependence. For that purpose we employ the emcee sampler with narrow prior distribution

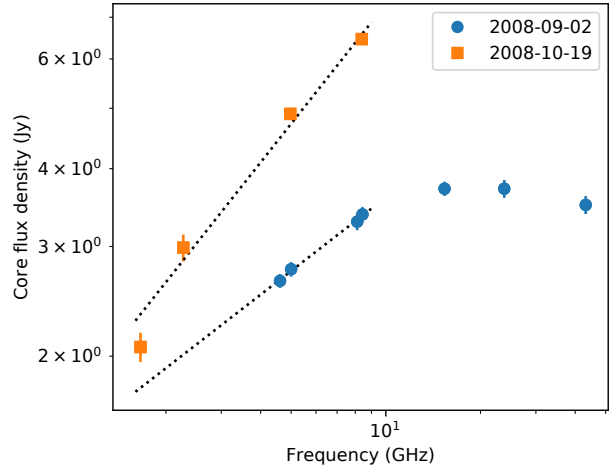


Figure 7. The core spectra for two epochs during the flare.

for $k_t = k_w = 0.8 \pm 0.1$ and obtain the resulting distributions of the other two parameters, yielding $a_t = 80 \pm 14$, and $b_t = -3 \pm 2$ days.

The core spectrum is shown on Figure 7 for two multi-frequency experiments (the core flux density at a given band is assumed to remain constant during the experiment, as well as shift of the core is neglected). The optically thick spectral index increases from $\alpha_1 = 0.39 \pm 0.09$ to $\alpha_2 = 0.64 \pm 0.05$, which might be related to the fact that peak at lower frequencies is lagged with respect to higher. We also discuss possible influence of adiabatic losses in Section 9.

7 BRIGHTNESS TEMPERATURE AND DOPPLER FACTOR

7.1 Ground-based VLBI

The apparent brightness temperature of a jet component in the source frame can be estimated using the obtained models (Kovalev et al. 2005):

$$T_b = 1.22 \cdot 10^{12} \frac{S(1+z)}{\nu^2 W_{maj} W_{min}} (K), \quad (4)$$

where S – flux density in Jy, W_{maj} and W_{min} – major and minor apparent size in mas (FWHM of Gaussian model), z – redshift, and ν – observing frequency in GHz.

On the other hand it is possible to estimate the so called variability brightness temperature in the source frame within the assumption that the variability time scale t_{var} corresponds to the light-crossing time of the component size (Hovatta et al. 2009):

$$T_{b,var} = 1.05 \cdot 10^8 \frac{D_\ell^2 S_{obs}}{(1+z)\nu^2 t_{var}^2} (K), \quad (5)$$

where D_ℓ – luminosity distance in Mpc, S_{obs} – flux density in Jy, ν – observations frequency in GHz, t_{var} – variability timescale in years.

T_b and T_{var} are measured experimentally and can be

expressed through an intrinsic brightness temperature, amplified by Doppler boosting (e.g. Kellermann et al. 2007):

$$\begin{cases} T_b = \delta T_{int} \\ T_{b,var} = \delta^3 T_{int}, \end{cases} \quad (6)$$

where δ is Doppler factor. System solution gives δ and T_{int} .

We adopt the following parameters: $D_\ell = 6142$ Mpc, $z = 0.94$, $S_{obs} = 4.7$ Jy – peak value of the core flux density during G-flare, and $t_{var} = 0.09$ yr – timescale of the core variability during G-flare. Note, that its profile has a plateau and differs from the two-sided exponential. Moreover, the flare decays faster than rises. We estimate the scale using time intervals and flux change various observations i, j during the flare as $t_{var} = |(t_i - t_j)/\ln(S_i/S_j)|$ taken on the flare decay (epoch 2008-11-03).

We obtain $T_{b,var} = 6.4 \cdot 10^{14}$ K and $T_b = 1.5 \cdot 10^{12}$ K, which yields to $\delta \approx 21$, and $T_{int} \approx 7 \cdot 10^{10}$ K. This value is close to the equipartition brightness temperature $T_{eq} \approx 5 \cdot 10^{10}$ K, suggested by Readhead (1994).

In Figure 8 the core flux density is shown along with derived T_b . Note that during the flares (2008 and 2015) brightness temperature increases by a factor ~ 2 .

Here we use a self-consistent system to estimate Doppler factor and intrinsic brightness temperature, considering the size and variability timescale of the same region.

7.2 RadioAstron

Assuming that the brightness distribution has a Gaussian profile we estimate the lower limit of T_b following Lobanov (2015):

$$T_{b,min} = \frac{\pi e}{2k_B} B^2 V_B \approx 3.09 \left(\frac{B}{km} \right) \left(\frac{V_B}{mJy} \right) [K], \quad (7)$$

where k_B is Boltzmann constant, B – baseline projection, V_B – visibility amplitude, measured on that baseline.

We also estimate T_b using the size inferred from modeling the visibility amplitudes on ground-ground and ground-space baselines with a circular Gaussian profile. T_b and size estimates are shown in columns (5–6) in Table 3. The estimates of T_b are plotted in Figure 8 with circles.

The highest brightness temperature estimate comes from the fringe detection at 26 Earth diameters baseline at 5 GHz. The longest baseline in units of wavelengths is 14 $G\lambda$ achieved at 22 GHz. The brightness temperature measured by RadioAstron is about an order of magnitude higher than that obtained from VLBA observations (Figure 8).

Among possible reasons and explanations of ultra-high apparent brightness temperatures are the following: i) the real jet speed is much higher than that derived from kinematics of components; ii) continuous injection or reacceleration of relativistic electrons that compensates the inverse Compton losses; iii) synchrotron emission of relativistic protons; iv) exotic models like mono-energetic spectrum of particles, etc. However, all these models come into collision with observational facts. See also discussion by Kovalev et al. (2016), who reported similar extreme brightness temperatures in blazar 3C 273.

On Figure 9 the brightness temperature measurements by RadioAstron and VLBA are plotted against the baseline.

Table 3. RadioAstron observations of 0235+164. Columns are: (1) Date, (2) Band, (3) Projected baseline (in Earth diameters), (4) Lower limit of brightness temperature, (5) Estimate of brightness temperature, (6) Estimate of circular Gaussian component size.

Date (1)	Band (2)	D/D_\oplus (3)	T_b^{min} (K) (4)	T_b^{est} (K) (5)	W (μas) (6)
2012-12-13	C	7.7	$2.0 \cdot 10^{12}$	$3.8 \cdot 10^{12}$	111.2
2012-12-15	C	14.9	$2.2 \cdot 10^{12}$	$1.0 \cdot 10^{13}$	70.3
2012-12-15	K	14.8	$9.2 \cdot 10^{12}$	$1.6 \cdot 10^{13}$	14
2012-12-16	C	18.7	$4.5 \cdot 10^{12}$	$1.8 \cdot 10^{13}$	54.4
2013-08-27	C	2.2	$3.9 \cdot 10^{11}$	$5.8 \cdot 10^{11}$	366.5
2013-08-27	L	2.8	$1.2 \cdot 10^{12}$	$1.3 \cdot 10^{12}$	470.6
2015-01-15	L	19.8	$1.5 \cdot 10^{12}$	$1.0 \cdot 10^{13}$	163.8
2015-12-16	C	8.7	$7.4 \cdot 10^{12}$	$1.2 \cdot 10^{13}$	92.9
2015-12-17	C	16.4	$7.8 \cdot 10^{12}$	$3.2 \cdot 10^{13}$	62.5
2015-12-29	C	25.5	$7.9 \cdot 10^{12}$	$4.9 \cdot 10^{13}$	43.0
2016-01-09	C	14.5	$1.2 \cdot 10^{13}$	$2.6 \cdot 10^{13}$	61.3
2016-01-29	C	8.9	$4.1 \cdot 10^{12}$	$1.3 \cdot 10^{13}$	108.2

This dependence (the absence of plateau) implies that there might be extremely compact jet components which can not be completely resolved even at baselines of $14 G\lambda$! The estimated size of these features is plotted on Figure 10 for 6 cm band. One can see, that the slope is close to formal interferometer resolution relation (wavelength over the baseline). The fit coefficient 5.5 ± 0.6 cm coincides with the observations wavelength. The size of $14 \mu\text{as}$ obtained at 1.35 cm by RadioAstron will fall exactly on the fitted line if corrected for the band frequency (factor $6/1.35$). The size estimated by 6 cm VLBA implies that there is a plateau of the apparent source size at small baselines (less than two Earth diameters). This indicates the presence of two scales in the source structure. The first one is what we call the “core”, and which might be resolved by ground-based facilities. The second is ultra-compact, less than $10 \mu\text{as}$ (or 0.1 pc), which remains unresolved even at longest ground-space baselines. The latter might be related to compact shocks or plasma blobs crossing the photosphere. The observed brightness temperatures $> 10^{13}$ K implies that a feature with size $\sim 10 \mu\text{as}$ must have flux density of $\gtrsim 0.03$ Jy at 6 cm.

A comprehensive analysis of interstellar scintillations (ISS) in 0235+164 performed by Rickett et al. (2006) gives the same estimates of the size and flux density of the ultra-compact jet feature (1992–1993 epochs). The authors found the increase of ISS amplitude during two major outbursts in the source (C and D in our notation) and suggest, that the compact features might be associated with the newborn jet components. These components travel downstream the jet and expand. The ISS of such a component has enough amplitude to produce apparent brightness temperatures of $\sim 10^{14}$ K at 2–8 GHz (Rickett et al. 2006).

One can see, that generally the measured brightness temperatures are higher when the source is in a flaring state

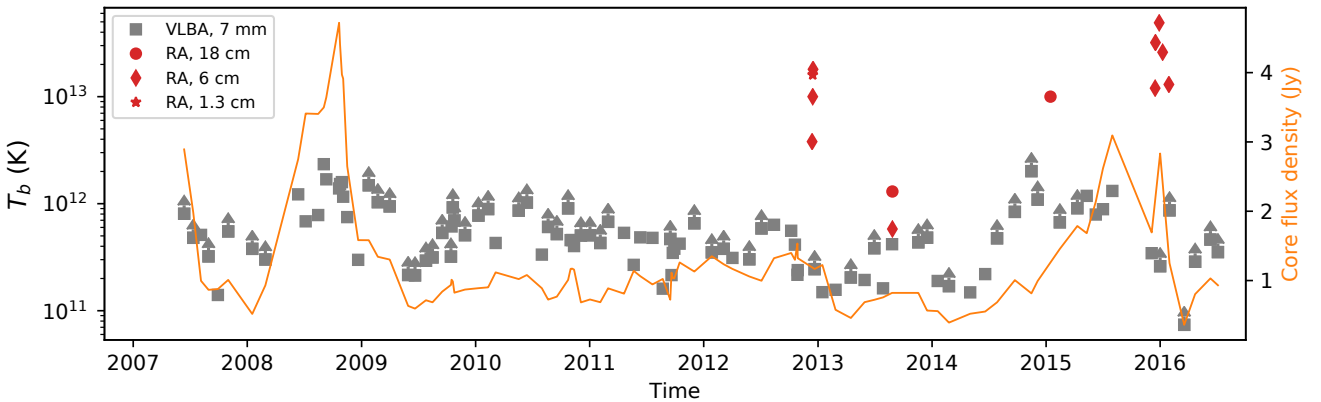


Figure 8. Brightness temperature by VLBA at 7 mm and RadioAstron at 18, 6, 1.35 cm. Arrows mark T_b estimated using the resolution limits. The curve shows core flux density (right axis).

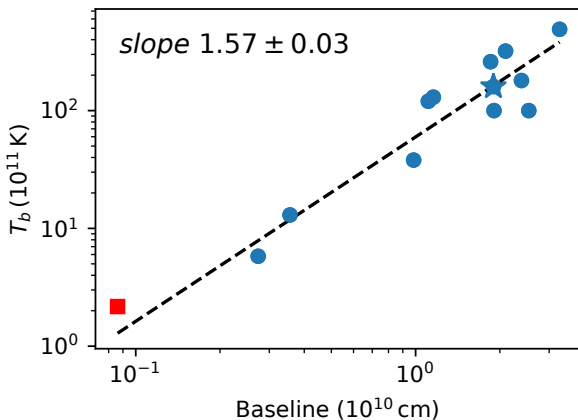


Figure 9. Brightness temperature measured by RadioAstron vs. the baseline (Table 3). Circles represent T_b at 6 and 18 cm, while the star – at 1.35 cm wavelengths. The square marks median T_b detected by ground-based 7 mm VLBA at the baseline 8600 km. The best linear fit is shown with the dashed line and its slope presented in the upper left corner.

(Figure 8). However, the high values appear during the quiescent states as well, suggesting that the bright compact features can occur in the jet without a prominent flare. Our quasi-simultaneous estimates of T_b at 1.35 and 6 cm (2012–12–15 epoch, Table 3) imply the spectral index of the associated component about +0.15, close to that of the core at these frequencies.

Therefore, the high brightness temperatures measured by RadioAstron in 0235+164 can be associated with the occurrence of extremely compact ($< 10\mu\text{as}$) features in the jet of the source. These features arise both in an active and a quiescent flaring states. Hence, their relation to the VLBI components is debated. Scintillation of these features at cm-wavelengths might lead to the observed variations of T_b . Moreover, if there are many such components at a time, they might produce a complex interferometric picture, i.e.

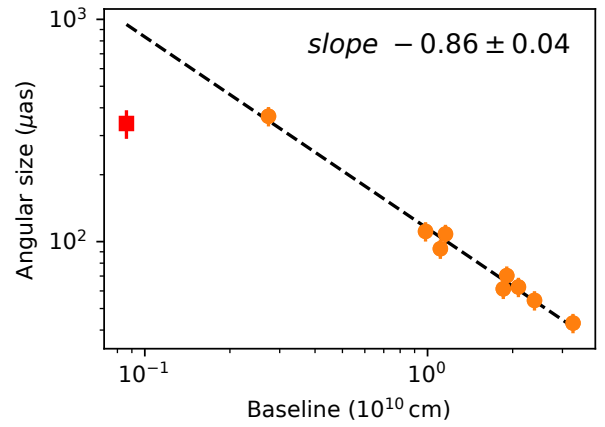


Figure 10. The source angular size estimated by fitting RadioAstron visibility amplitudes at 6 cm (circles, Table 3). The square marks the size of 6 cm core from ground-based VLBA measurements (Table 1). The best linear fit is shown with the dashed line and its slope presented in the upper right corner.

at some baselines projections/extension one can obtain a surprising interferometer response.

Note, that at 1.35 cm the interstellar scattering does not seem to play significant role in the observed source structure (Johnson et al. 2016). We also do not expect strong scintillations at 22 GHz. Then, the variations of T_b (if any detected with the same interferometer configuration) at these frequencies must be attributed to the intrinsic evolution of the compact jet features discussed.

8 JET STRUCTURE

8.1 Image stack

As noted in Section 1 the structure of 0235+164 is extremely pure and unstable. It is very difficult to determine jet geometrical characteristics from a single VLBI observation.

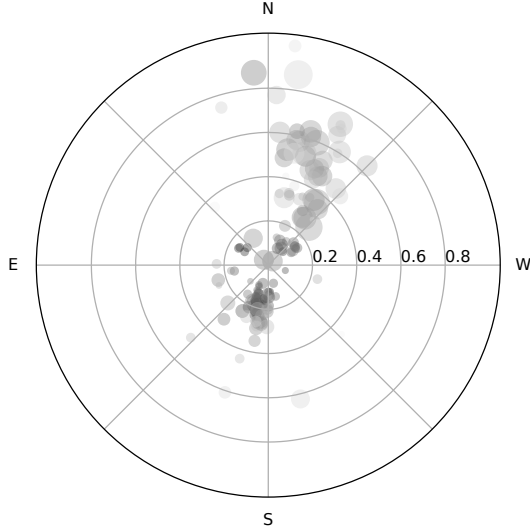


Figure 11. The model components within 1 mas of the core, aligned relative the position of the core (not plotted). The circles size and color intensity are proportional to the size and flux density of the components.

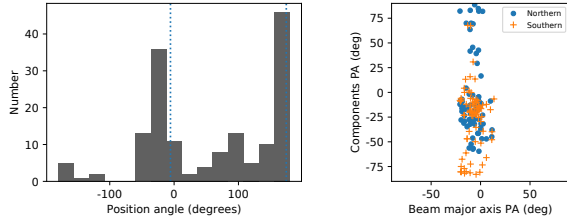


Figure 12. The distribution of the components position angles. Vertical lines show the median of beam major axis orientation. On the right panel position angle of the components (reduced to $[-90^\circ, 90^\circ]$) vs. the position angle of the beam major axis.

Moreover, even the direction of the jet is not clear. In Figure 11 all our models of the 100 7 mm VLBA observations are plotted with respect to the core position (the core is not shown). It is clearly seen that the components tend to concentrate almost symmetrically at two directions. We check if the position angles of the components (median -28° and 162°) correlate with the major axis of the synthesized beam (median -6°). They are found to be close but not coincide, neither showing correlation (Figure 12). So the beam does not seem to be responsible for the observed phenomena. Another support comes from the fact that the size of the components increases with distance from the core both in southern and northern directions. Moreover, in the northern part there are farther and larger components (see Figure 13). We interpret this as a bend of the outflow from south to north, so that the younger (closer to the central engine) jet is observed southwards and the older (more extended and prominent) is seen northwards of the core.

We combine the 100 7 mm VLBA maps (obtained in independent experiments) aligned by the core position into a

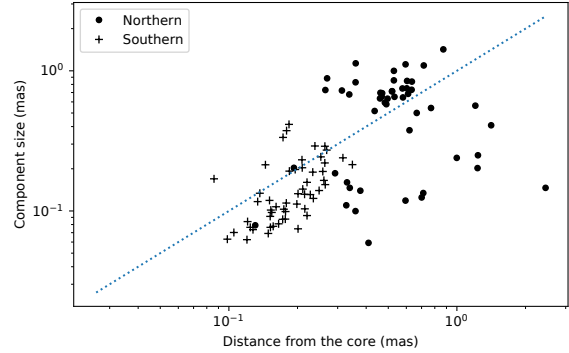


Figure 13. Size of the components vs. their distance from the core. The dotted line represents equality.

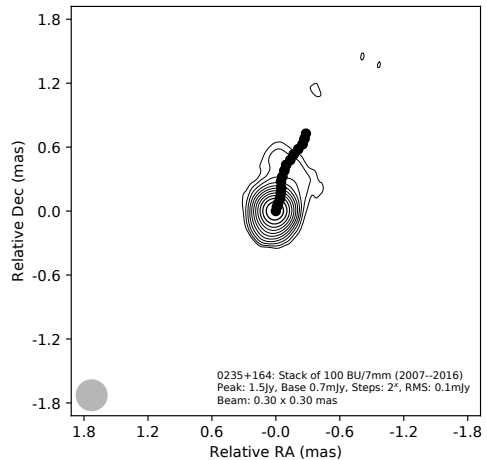


Figure 14. The stacked map of 0235+164 at 7mm. Black circles show the ridge line. Grey circle in the lower left corner shows the beam.

stack image to increase dynamic range. This allows us to see the jet and construct the ridge line up to ~ 0.8 mas north-northwest of the core as shown in Figure 14 (the southern ridge line would be too short to perform any calculations). The intensity along transverse jet slices measured down the ridge line is modeled with Gaussian profile, whose width being deconvolved with the beam represents the real jet width w . Apparent opening angle φ is then estimated as $\varphi = 2 \arctan(w/2l)$, where l is distance along the ridge line. The jet profile ($w/2$ vs. l) is shown in Figure 15. Assuming conical geometry we find $\varphi_{43} = 60^\circ \pm 5^\circ$. It is two times higher than the value obtained by Pushkarev et al. (2017) for stacked image at 15 GHz on larger scales ($\varphi_{15} = 30^\circ$ on about 2 mas), suggesting that the jet is collimated somewhere within ~ 1.5 mas of the core. At lower frequency (1.4 GHz, tens mas) the VLBA stacked image shows that jet changes its direction to north-northeast (Pushkarev et al. 2017) keeping the same opening angle $\sim 30^\circ$.

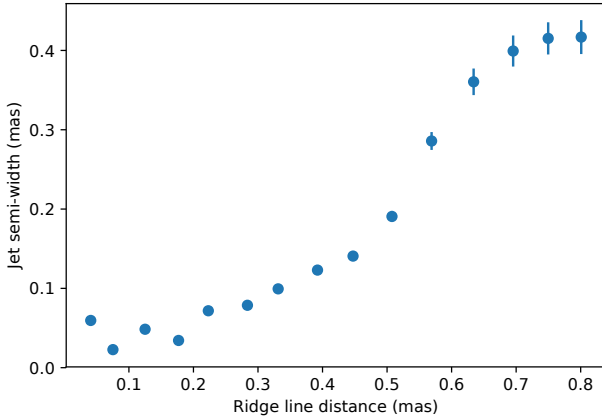


Figure 15. Jet half-width vs distance along the ridge line.

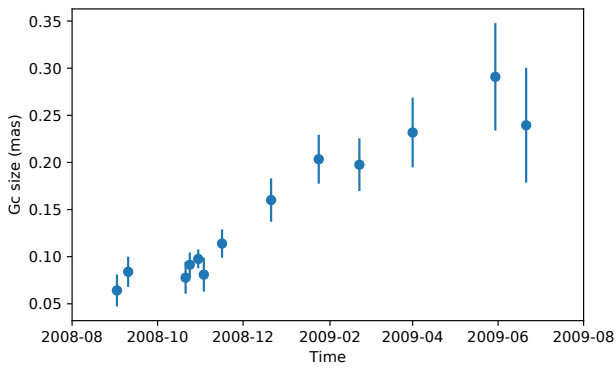


Figure 16. The size of Gc vs time.

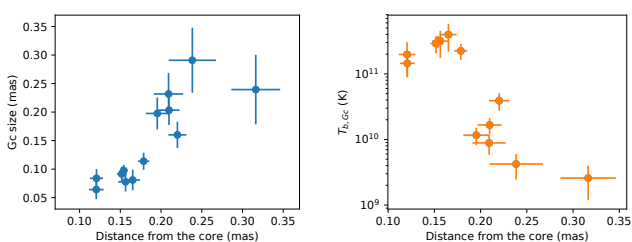


Figure 17. The size and apparent brightness temperature of Gc vs. its separation from the core.

8.2 Gc component

The G-flare (see Figure 2) is accompanied by a bright feature (Gc hereafter) located to the south-southeast from the core and traveling with apparent superluminal velocity (see below). It has been also studied by Agudo et al. (2011), who interpreted it as a moving transverse shock.

In Figure 18 the trajectory of Gc is shown relative to the core position. The mean proper motion of Gc relative to the core is $\mu = 0.20 \pm 0.03$ mas/yr, which corresponds to apparent speed $\beta_{app} = 10 \pm 1.6 c$. The position and speed of Gc

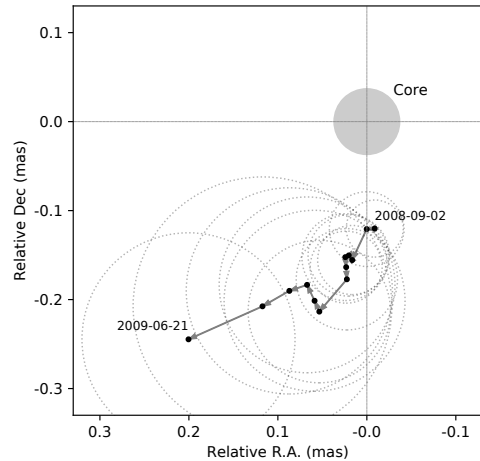


Figure 18. Trajectory of the Gc component during Sep 2008 – Jun 2009 at 43 GHz. Dots, arrows and open circles show the position, path and size of the Gc. The core is at (0,0) and its median major axis shown with gray circle.

is consistent with its ejection in Jan 2008, at the beginning of the core (and total flux) flare.

Using equations (4–6) we estimate the brightness temperature and Doppler factor of Gc. During the flare peak $T_{b,Gc} \approx 4 \cdot 10^{11}$ K (Figure 17). Taking the variability timescale at Gc-flare peak $t_{var,Gc} = 0.1$ yr (estimated in the same way as for the core at flare decay in Nov 2008) and corresponding $T_{var,Gc} = 2.4 \cdot 10^{14}$ K we obtain $T_{b,int,Gc} \approx 10^{10}$ K, $\delta_{Gc} \approx 24$.

The Lorentz factor and the viewing angle can be estimated using the following equations:

$$\Gamma = \frac{\beta_{app}^2 + \delta^2 + 1}{2\delta}, \quad \theta = \arctan \frac{2\beta_{app}}{\beta_{app}^2 + \delta^2 - 1}, \quad (8)$$

which give $\Gamma \approx 14$ and $\theta \approx 1.7^\circ$.

The slope of Gc size vs. distance from the core is 1.2 ± 0.4 implying the conical angle $\varphi_{Gc} \approx 62^\circ$, which coincides with the opening angle φ obtained from the stacked image in the northern jet. The intrinsic opening angle of the jet is then $\varphi_{int} = \varphi_{Gc} \sin \theta \approx 2^\circ$.

If the viewing angle of the inner jet (in the core region) is the same as of Gc, then the Lorentz factor and apparent speed in that region are also kept as $\delta_{core} \approx \delta_{Gc}$.

Since the distance between the core and Gc is less than the beam size, one can argue that this is an artifact. However, the evolution of its size and brightness temperature with time and distance from the core (Figures 16, 17) as well as its birth date suggest that Gc is indicative on the existence of this component.

9 CORE SHIFT AND PHYSICAL PARAMETERS

Within the photosphere interpretation of the core, its apparent shift Δr and change of transverse size ΔW_{min} in

conical jet are related through the apparent opening angle φ as $\Delta r = \Delta W_{min}/2 \tan \varphi/2$. Here we assume that major and minor core axes are aligned with axial and transverse directions of the inner jet, which is typical for blazars (Kovalev et al. 2005).

Therefore, it is easy to estimate the core shift for a given frequency pair. For example, the shift between the core at 15 and 8 GHz is then $\Delta r_{15-8} \approx 0.03$ mas, which is several times lower than the median value (0.128 mas) obtained by Pushkarev et al. (2012) for these frequencies. The smaller core shift value is expected for the source having small viewing angle. The core shift between 15 and 5 GHz is $\Delta r_{15-5} \approx 0.1$ mas.

Consider standard scalings for the particles density $N = N_1(r/r_1)^{-n}$ and magnetic field strength $B = B_1(r/r_1)^{-m}$, where index 1 refers to values at 1 pc from the central engine. In freely expanding jet (without ambient medium pressure) the power indices m, n can be linked through the measured index k and optically thin spectral index α (Konigl 1981)⁸:

$$k = \frac{5 - 2\alpha}{(3 - 2\alpha)m + 2n - 2} \quad (9)$$

Further we discuss the equipartition regime, when the energy density of relativistic electrons equals to that of the magnetic field. We also consider other scenario, where the conical jet with transverse magnetic field undergoes adiabatic losses following Marscher (1980).

9.1 Equipartition case

Estimation of physical parameters can be performed taken into account the fact that the core brightness temperature is close to the equipartition value $T_{b,eq} \sim 10^{10.5}$ K. Equipartition between particles and magnetic field energy density implies that $n = 2m$, and from (9) for $k = 0.8 \pm 0.1$ and $\alpha = -0.5$ we obtain $m = 1.2 \pm 0.1$, $n = 2.4 \pm 0.2$. Note, that the dependence of the parameters on α is weak, and using $\alpha = -0.75$ changes the above results insignificantly.

The measure of core offset for a given frequency pair ν_1, ν_2 can be introduced following Lobanov (1998):

$$\Omega = 4.85 \cdot 10^{-9} \frac{\Delta r_{mas} D_\ell}{(1+z)^2} \left(\frac{\nu_1^k \nu_2^k}{\nu_2^k - \nu_1^k} \right), \quad (10)$$

where D_ℓ is the luminosity distance in pc, Δr_{mas} – the core shift in mas. Then magnetic field strength at 1 pc:

$$B_1 \approx 0.025 \left(\frac{\Omega^{3/k} (1+z)^2}{\delta^2 \phi \sin^{3/k-1} \theta} \right)^{1/4}, \quad (11)$$

where θ is the jet viewing angle, ϕ is the jet half opening angle and δ is the Doppler factor. Substitution of the parameters gives $B_1 \approx 1.3$ G. De-projected distance from the central engine to the core at a frequency ν is then:

$$r_{core}(\nu) = \frac{\Omega}{\sin \theta} \nu^{-k} \quad (12)$$

E.g., the core at 7 mm is located at $r_{core,43} \approx 10.5$ pc,

⁸ Note, that throughout this paper k is defined as k^{-1}

while the core at 2.3 GHz is more than 100 pc downstream from the jet apex. The magnetic field in the 43 GHz core is $B_{7mm\ core} \approx 0.1$ G.

9.2 Adiabatic case

The inverted spectrum of the core at lower frequencies (Figure 7) may also be related to the adiabatic losses, which might dominate in the jet on parsec scales (Marscher 1980). Assume $m = 1$, as expected for the transverse magnetic field (Blandford & Rees 1974), and $n = 2/3(2-s)$, where s – is the slope of the electron energy distribution's power law. The optically thin spectral index $\alpha = (s+1)/2$. Then the solution of Eq. (9) gives $s = -2.15$. This value is very close to that predicted by models of electrons acceleration by relativistic shocks in AGN jets (Kirk et al. 2000). Note, that the dependence of s on the observed index k is very strong, e.g. $s(k=0.7) = -3.4$ and $s(k=0.9) = -1.5$. If we assume $m = 2$ instead (the longitudinal magnetic field), we obtain unrealistic slope $s(k=0.8) = -0.16$.

Therefore, both equipartition and adiabatic cases suggest m close to 1, and reject $m = 2$. This implies dominance of the transverse component of the magnetic field.

9.3 Jet speed

We assume, that the distance between the core at given two frequencies corresponds to the peak-to-peak time delay and the speed of the flow (i.e. the apparent core shift can be expressed through the delay and proper motion as $\Delta r = \mu \Delta T$). For $\Delta r_{15-5} = 0.1$ mas and $\Delta T_{G,15-5} = 14$ days we obtain $\mu = 2.6$ mas/yr (130c in the source redshift), which is an order of magnitude higher than the proper motion found for the Gc component. Then the bulk flow speed differs from the pattern speed in the jet of 0235+164, which must be studied additionally.

10 CONCLUSIONS

Application of GPR method allows us to localize the peaks of the flares with accuracy better than would be possible with the traditional cross-correlation techniques, and obtain reliable estimates of the multi-frequency time delays. The dependencies of time lags and core size on frequency suggest that the synchrotron self-absorption dominates the jet's radio emission at cm- and mm-wavelengths. Power index k_t differs significantly from one flare to another, suggesting changes in physical conditions or geometrical characteristics of the jet. The total flux profile of the 2008 flare at mm wavelengths is found to be a sum of the core and the component flux density variations. Such cases can also affect the measured difference of k_t , and must be taken into account for estimates of variability timescales, brightness temperature, Doppler factor, and core shift.

We implement a self-consistent method to estimate Doppler factor and intrinsic brightness temperature of the core using the size and variability scale of the same region. The obtained value of $T_{b,int}$ is close to one expected in equipartition regime. The brightness temperature measured using ground-based VLBI increases by a factor 2 during the flares, but still is much lower than one obtained with

the space interferometer RadioAstron, where visibility amplitudes 50 – 100 mJy are detected on baselines up to 14 G λ . We find an evidence for presence of ultra-compact ($< 10 \mu\text{as}$) features, which may arise in the source even during its quiescent states. These spikes might demonstrate fast flux variations at cm-wavelengths via ISS mechanism, in good agreement with the observed intra-day variability of 0235+164.

The Doppler factor of the superluminal component Gc estimated from its kinematic analysis is in good agreement with one, found for the core from ground-based VLBA brightness temperature measurements. The estimated birth epoch of Gc as well as increase of its size with time and distance from the core, provide strong support for it to be a real jet component. The two prevalent directions in the scattering of the components at 7 mm are probably caused by jet bend from south to north. The brighter, more compact and closer to the core components are observed in the southern jet during all the period studied, which provide strong support for this scenario. The estimates of the opening angle of the southern (from the Gc component size) and the northern (from stacked image) jet also suggest that its direction is changed, but not the opening angle. Millimeter interferometric observations with higher resolution in north-south direction would shed more light on this enigmatic structure. The intrinsic opening angle of the outflow cone is close to the viewing angle within 0.7 mas of the central engine, yielding to the additional scattering of position angles of the observed components. The flow is collimated, and on larger scales ($> 1 \text{ mas}$) its opening angle becomes smaller than the viewing one. We estimate high, but not extreme values of Lorentz factor $\Gamma = 14$ and Doppler factor $\delta = 21$, and moderate viewing angle $\theta = 1.7^\circ$.

Based on the derived jet geometry we estimate the core shift magnitude in the jet of 0235+164. We consider the equipartition and adiabatic scenarios, which adequately describe the observational data. Both cases imply the dominance of a transverse magnetic field component. Within the equipartition assumption we derive the gradients of magnetic field strength and electron density in the jet, as well as the linear scales corresponding to the core at each frequency. Magnetic field in the 7 mm core $B_{7\text{mm}} \approx 0.1 \text{ G}$ is typical reported for the blazars.

ACKNOWLEDGMENTS

We thank Alexander Pushkarev, Alan Marscher and David Jauncey for the useful comments. The research was supported by Russian Science Foundation (project 16-12-10481). It makes use of 43 GHz VLBA data from the **VLBA-BU Blazar Monitoring Program** (VLBA-BU-BLAZAR; <http://www.bu.edu/blazars/VLBAproject.html>), funded by NASA through the Fermi Guest Investigator Program. The VLBA is an instrument of the Long Baseline Observatory. The Long Baseline Observatory is a facility of the National Science Foundation operated by Associated Universities, Inc. The **European VLBI Network** is a joint facility of independent European, African, Asian, and North American radio astronomy institutes. Scientific results from data presented in this publication are derived from the following EVN project code(s): EK028. The study

has made use of data from the **OVRO** 40-m monitoring program (Richards et al. 2011) which is supported in part by NASA grants NNX08AW31G, NNX11A043G, and NNX14AQ89G and NSF grants AST-0808050 and AST-1109911. The **RadioAstron** project is led by the Astro Space Center of the Lebedev Physical Institute of the Russian Academy of Sciences and the Lavochkin Scientific and Production Association under a contract with the Russian Federal Space Agency, in collaboration with partner organizations in Russia and other countries. Results of optical positioning measurements of the Spektr-R spacecraft by the global MASTER Robotic Net (Lipunov et al. 2010), ISON collaboration, and Kourouva observatory were used for spacecraft orbit determination in addition to mission facilities.

References

- Abraham R. G., Crawford C. S., Merrifield M. R., Hutchings J. B., McHardy I. M., 1993, *ApJ*, **415**, 101
 Ackermann M., et al., 2012, *ApJ*, **751**, 159
 Agudo I., et al., 2011, *ApJ*, **735**, L10
 Altschuler D. R., Gurvits L. I., Alef W., Dennison B., Graham D., Trotter A. S., Carson J. E., 1995, *A&AS*, **114**, 197
 Ambikasaran S., Foreman-Mackey D., Greenard L., Hogg D. W., O’Neil M., 2014, preprint, ([arXiv:1403.6015](https://arxiv.org/abs/1403.6015))
 Blandford R. D., Königl A., 1979, *ApJ*, **232**, 34
 Blandford R. D., Rees M. J., 1974, *MNRAS*, **169**, 395
 Burbidge E. M., Beaver E. A., Cohen R. D., Junkkarinen V. T., Lyons R. W., 1996, *AJ*, **112**, 2533
 Chu H. S., Baath L. B., Rantakyrö F. T., Zhang F. J., Nicholson G., 1996, *A&A*, **307**, 15
 Cohen R. D., Smith H. E., Junkkarinen V. T., Burbidge E. M., 1987, *ApJ*, **318**, 577
 Cordes J. M., Lazio T. J. W., 2002, ArXiv Astrophysics e-prints, Edelson R. A., Krolik J. H., 1988, *ApJ*, **333**, 646
 Fomalont E. B., 1999, in Taylor G. B., Carilli C. L., Perley R. A., eds, Astronomical Society of the Pacific Conference Series Vol. 180, Synthesis Imaging in Radio Astronomy II. p. 301
 Foreman-Mackey D., 2016, *The Journal of Open Source Software*, **24**
 Foreman-Mackey D., Hogg D. W., Lang D., Goodman J., 2013, *PASP*, **125**, 306
 Frey S., et al., 2000, *PASJ*, **52**, 975
 Gabuzda D. C., Cawthorne T. V., 2000, *MNRAS*, **319**, 1056
 Georganopoulos M., Marscher A. P., 1996, in Miller H. R., Webb J. R., Noble J. C., eds, Astronomical Society of the Pacific Conference Series Vol. 110, Blazar Continuum Variability. p. 262
 Greisen E. W., 1990, in G. Longo & G. Sedmak ed., Acquisition, Processing and Archiving of Astronomical Images. pp 125–142
 Hada K., Doi A., Kino M., Nagai H., Hagiwara Y., Kawaguchi N., 2011, *Nature*, **477**, 185
 Hastie T., Tibshirani R., Friedman J., 2009, The Elements of Statistical Learning: Data Mining, Inference, and Prediction, second edn. Springer, <http://web.stanford.edu/~hastie/ElemStatLearn>
 Hirotani K., 2005, *ApJ*, **619**, 73
 Högbom J. A., 1974, *A&AS*, **15**, 417
 Hovatta T., Valtaoja E., Tornikoski M., Lähteenmäki A., 2009, *A&A*, **494**, 527
 Johnson M. D., et al., 2016, *ApJ*, **820**, L10
 Jones D. L., Baath L. B., Davis M. M., Unwin S. C., 1984, *ApJ*, **284**, 60

- Jorstad S. G., Marscher A. P., Mattox J. R., Wehrle A. E., Bloom S. D., Yurchenko A. V., 2001, *ApJS*, **134**, 181
- Karamanavis V., et al., 2016, *A&A*, **590**, A48
- Kardashev N. S., et al., 2013, *Astronomy Reports*, **57**, 153
- Keimpema A., et al., 2015, *Experimental Astronomy*, **39**, 259
- Kellermann K. I., et al., 2007, *Ap&SS*, **311**, 231
- Kirk J. G., Guthmann A. W., Gallant Y. A., Achterberg A., 2000, *ApJ*, **542**, 235
- Komatsu E., et al., 2009, *ApJS*, **180**, 330
- Konigl A., 1981, *ApJ*, **243**, 700
- Kovalev Y. Y., et al., 2005, *AJ*, **130**, 2473
- Kovalev Y. Y., et al., 2016, *ApJ*, **820**, L9
- Kraus A., et al., 1999, *A&A*, **344**, 807
- Kudryavtseva N. A., Gabuzda D. C., Aller M. F., Aller H. D., 2011, *MNRAS*, **415**, 1631
- Kutkin A. M., et al., 2014, *MNRAS*, **437**, 3396
- Likhachev S. F., Kostenko V. I., Girin I. A., Andrianov A. S., Zharov V. E., Rudnitskiy A. G., 2017, preprint, ([arXiv:1706.06320](#))
- Lipunov V., et al., 2010, *Advances in Astronomy*, **2010**, 349171
- Lobanov A. P., 1998, *A&A*, **330**, 79
- Lobanov A., 2015, *A&A*, **574**, A84
- MacKay D. J., 2003, *Information Theory, Inference and Learning Algorithms*. Cambridge University Press
- Marciaide J. M., Shapiro I. I., 1984, *ApJ*, **276**, 56
- Marscher A. P., 1980, *ApJ*, **235**, 386
- Marscher A. P., 2006, in P. A. Hughes & J. N. Bregman ed., American Institute of Physics Conference Series Vol. 856, Relativistic Jets: The Common Physics of AGN, Microquasars, and Gamma-Ray Bursts. pp 1–22, [doi:10.1063/1.2356381](#)
- Marscher A. P., 2008, in T. A. Rector & D. S. De Young ed., Astronomical Society of the Pacific Conference Series Vol. 386, Extragalactic Jets: Theory and Observation from Radio to Gamma Ray. p. 437
- Max-Moerbeck W., Richards J. L., Hovatta T., Pavlidou V., Pearson T. J., Readhead A. C. S., 2014, *MNRAS*, **445**, 437
- Napier P. J., 1994, in Robertson J. G., Tango W. J., eds, IAU Symposium Vol. 158, Very High Angular Resolution Imaging. p. 117
- Nilsson K., Charles P. A., Pursimo T., Takalo L. O., Sillanpaeae A., Teerikorpi P., 1996, *A&A*, **314**, 754
- Peterson B. M., Wanders I., Horne K., Collier S., Alexander T., Kaspi S., Maoz D., 1998, *PASP*, **110**, 660
- Petrov L., Kovalev Y. Y., Fomalont E. B., Gordon D., 2011, *AJ*, **142**, 35
- Pushkarev A. B., Kovalev Y. Y., 2015, *MNRAS*, **452**, 4274
- Pushkarev A. B., Hovatta T., Kovalev Y. Y., Lister M. L., Lobanov A. P., Savolainen T., Zensus J. A., 2012, *A&A*, **545**, A113
- Pushkarev A. B., Kovalev Y. Y., Lister M. L., Savolainen T., 2017, preprint, ([arXiv:1705.02888](#))
- Pyatunina T. B., Kudryavtseva N. A., Gabuzda D. C., Jorstad S. G., Aller M. F., Aller H. D., Teräsranta H., 2007, *MNRAS*, **381**, 797
- Rasmussen C. E., Williams C. K. I., 2005, *Gaussian Processes for Machine Learning (Adaptive Computation and Machine Learning)*. The MIT Press
- Readhead A. C. S., 1994, *ApJ*, **426**, 51
- Richards J. L., et al., 2011, *ApJS*, **194**, 29
- Rickett B. J., Lazio T. J. W., Ghigo F. D., 2006, *ApJS*, **165**, 439
- Shepherd M. C., 1997, in G. Hunt & H. Payne ed., Astronomical Society of the Pacific Conference Series Vol. 125, Astronomical Data Analysis Software and Systems VI. p. 77
- Sokolovsky K., 2011, PhD thesis, Max-Planck-Institut für Radioastronomie
- Sokolovsky K. V., Kovalev Y. Y., Lobanov A. P., Savolainen T., Pushkarev A. B., Kadler M., 2010b, ArXiv:1001.2591,
- Sokolovsky K. V., et al., 2010a, ArXiv:1006.3084,
- Sokolovsky K. V., Kovalev Y. Y., Pushkarev A. B., Lobanov A. P., 2011, *A&A*, **532**, A38
- Spinrad H., Smith H. E., 1975, *ApJ*, **201**, 275
- Stickel M., Fried J. W., Kuehr H., 1988, *A&A*, **198**, L13
- Valtaoja E., Lähteenmäki A., Teräsranta H., Lainela M., 1999, *ApJS*, **120**, 95
- Véron-Cetty M.-P., Véron P., 2010, *A&A*, **518**, A10
- Walker R. C., 1995, in Zensus J. A., Diamond P. J., Napier P. J., eds, *Astronomical Society of the Pacific Conference Series Vol. 82, Very Long Baseline Interferometry and the VLBA*. p. 247
- Webb J. R., Howard E., Benítez E., Balonek T., McGrath E., Shrader C., Robson I., Jenkins P., 2000, *AJ*, **120**, 41
- White R. J., Peterson B. M., 1994, *PASP*, **106**, 879
- Yang J., Gurvits L. I., Frey S., Lobanov A. P., 2009, in Proceedings of 10th Asian-Pacific Regional IAU Meeting, eds. Shuang Nan Zhang, Yan Li and Qing Juan Yu, National Observatories of China Press,